

SPATIOTEMPORAL DEEP LEARNING FOR PREDICTING MICROSTRUCTURE EVOLUTION IN LASER-BASED ADDITIVE MANUFACTURING

*Eva Fasting Narvestad (S250062), Andreas Wendelboe (S215489)
 Buster Bøgild Nielsen (S211548), Ong Jing Wei (S242672), Mads Sørensen (S215805)*

ABSTRACT

Laser-based additive manufacturing (LBAM) induces microstructural changes that influence the properties of the final material. In this project we develop deep learning models based on CNN-LSTM and PredRNN architectures for predicting temperature and microstructure spatiotemporal evolution during LBAM of steel from simulation data. The temperature prediction network (TempNet) first predicts the next-frame temperature for t_{+1} based on previous temperature history and its output conditions a second network (MicroNet) that predicts nine IPF microstructure channels. Our experiments demonstrate the feasibility of learning temperature progression and microstructural changes from limited simulation data.

1. INTRODUCTION

LBAM enables the production of complex components, where the moving laser creates a melt pool that drives solidification, grain growth, and crystallographic reorientation. The microstructure strongly influences the material's mechanical properties and reliability [1]. Physics simulations can compute the system dynamics but are computationally expensive. Deep learning models offer an alternative by learning the spatiotemporal behaviour of melt-pool dynamics.

The goal of this project is to develop deep learning models capable of predicting both temperature fields and microstructure spatiotemporal evolution during LBAM. We formulate two coupled prediction tasks: (1) predicting the next temperature frame t_{+1} given a sequence of past temperature frames, and (2) predicting the next t_{+1} Inverse Pole Figure (IPF)¹ fields conditioned on both historical IPF fields and temperature fields and the previous predicted t_{+1} temperature frame. These tasks are addressed using CNN-LSTM[2] and PredRNN [3] architectures, enabling the model to learn both spatial features and temporal dynamics.

¹IPFs are one way to describe or visualize part of a material's microstructure. IPF & microstructure will be used interchangeably.

2. METHODOLOGY

2.1. Dimensional reduction

The dataset consists of a large point cloud for all T timesteps. The point cloud is computationally impractical for training and the key variations relevant to melt pool evolution occur within a thin region around the melt boundary, meaning a full 3D representation is unnecessary to learn the system dynamics. To reduce spatial complexity, 2D planar slices are used as the model input. The XZ-plane is selected because the laser moves along the x-direction. When viewed along the x-axis (YZ-plane), the melt pool shows very limited variation, whereas the XZ-plane reveals its length, depth, and temporal changes clearly, making the XZ-plane the most information preserving slice for describing the dominant dynamics of the system [4].

A temporal reduction is applied as well. Long time sequences contain many redundant frames because the melt pool evolution is relatively smooth over short intervals, and changes occur mostly over limited time windows [5]. Feeding long sequences to the model increases the amount of parameters, computational cost and memory usage without providing proportional gains in predictive accuracy [3]. To address this, the input is restricted to a temporal window of length L , followed by one prediction frame. This preserves local temporal dynamics while discarding distant temporal context that contributes little to short-term predictions.

2.2. Dataset Preprocessing

The point cloud is provided as a CSV file in which each row corresponds to a mesh point and contains its coordinates (x, y, z) , temperature, nine IPF components, the origin index, and the grain identifier. The first preprocessing step reconstructs these point samples into tensors $\mathbf{X}_t \in \mathbb{R}^{D \times H \times W \times C}$, where each voxel stores $C = 10$ channels consisting of temperature and the nine IPF values. Training sequences are generated with a window size L over the temporal data. For each timestep t , this produces an input sequence $\mathbf{X}_{t-L+1:t}$ and a corresponding target frame $\mathbf{Y}_{t+1} = \mathbf{X}_{t+1}$. The data is finally normalized to the $[0, 1]$ range.

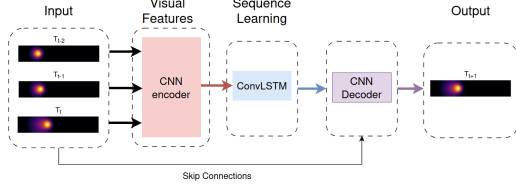


Fig. 1. CNN-LSTM high-level diagram for temperature prediction

2.3. Overall architecture

We adopt a baseline spatiotemporal model based on the CNN-LSTM architecture proposed by Shi et al. [2]. The system consists of two separate networks: a temperature predictor (*TempNet*) and a microstructure predictor (*MicroNet*). *TempNet* first processes a sequence of historical temperature frames to forecast the next temperature field. This predicted temperature state is effectively treated as a conditional prior for the second stage; it is encoded and inputted together with the latent spatiotemporal features of the historical microstructure sequence. This coupling ensures that the prediction of the nine IPF channels in *MicroNet* is explicitly driven by the temperature conditions of the melt pool.

2.4. Temperature Prediction model (*TempNet*)

TempNet follows a CNN-LSTM architecture, where a CNN extracts spatial features from each of the three temperature frames and an LSTM models their temporal evolution. Each frame is processed independently through a convolutional encoder ($1 \rightarrow 16 \rightarrow 32 \rightarrow 64$), which extracts hierarchical spatial features while preserving the 2D layout of the image. Intermediate encoder feature maps are stored as skip connections for later use in the decoder. The encoded feature maps from all input frames are stacked and passed through a ConvLSTM module, which maintains spatially structured hidden states and learns how the spatial patterns evolve over time. The ConvLSTM output provides a spatiotemporal representation corresponding to the final input frame. This representation is then upsampled through a multi-stage decoder to reconstruct the predicted next temperature frame. During decoding, the stored encoder feature maps are concatenated with the corresponding decoder layers, allowing the model to preserve fine-grained spatial detail in the prediction [6].

2.5. Microstructure prediction model

The *MicroNet* CNN-LSTM model predicts the next-frame nine-channel IPF fields and the temperature conditioned on the previous microstructure and temperature history. Each frame (10 channels: temperature + 9 IPF channels) is encoded with a CNN ($10 \rightarrow 16 \rightarrow 32 \rightarrow 64$) and downsampled before entering a ConvLSTM that captures temporal dependencies.

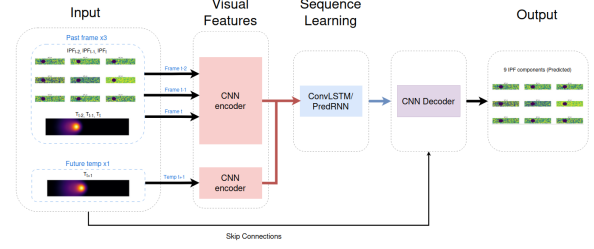


Fig. 2. CNN-LSTM & PredRNN high-level diagram for temperature prediction

The future-temperature frame is encoded separately with an identical encoder. The ConvLSTM output is decoded through a U-Net-style decoder to reconstruct the nine microstructure channels.

The PredRNN variant replaces the ConvLSTM with stacked Spatiotemporal LSTM layers. Encoded historical frames and skip connections follow the same setup as in the CNN-LSTM version. The final PredRNN state is fused with the encoded future-temperature features and decoded to produce the predicted microstructure channels.

3. EXPERIMENTS

3.1. Temperature prediction

The temperature prediction task was studied using several CNN-LSTM model variants with different training configurations and sequence lengths to assess their impact on prediction accuracy. The experiments varied the sequence input length (2, 3, and 4 frames), the number of convolutional layers, the number of ConvLSTM layers and the use of U-Net style skip connections. In addition, the impact of training hyper-parameters such as loss function, learning rate, number of epochs and dropout were examined. Table 2 reports the training and validation performance of the most important architectures used during model tuning. MSE was used as the primary optimization loss, while both MSE and MAE were used for evaluation. Adding skip connections significantly improved performance compared to the baseline model, reducing the validation MSE from 4002 to 1711. Increasing the convolutional depth to four layers further reduced the validation error to an MSE of 1051 and MAE of 19.03. The best overall training and validation performance was obtained with U-Net, four convolution layers and 2 LSTM layers (ID T4 in Table 3) and this was therefore kept as a new baseline for subsequent experiments. A visual comparisons between the initial baseline and the selected baseline can be seen in Figure 7 and Figure 8. The selected *TempNet* baseline was later used in a series of experiments to study the effect of temporal context length and hyperparameters, as reported in Section 3.3.1.

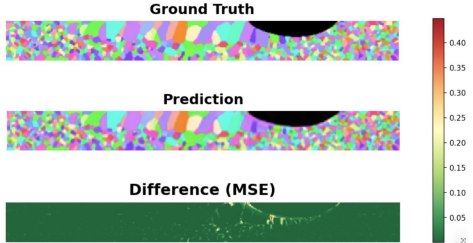


Fig. 3. CNN-LSTM with MSELoss prediction on the test set. $T = t_{23}$, y-axis slice index 47. Table 1, Model ID 5.

3.2. Microstructure prediction

Our initial implementation of MicroNet did not include any U-Net-style skip connections. We evaluated both the CNN-LSTM and PredRNN architectures using sequence lengths of 2, 3, 4, and 5. For CNN-LSTM, the best-performing configuration used a sequence length of 3, while PredRNN achieved its highest performance with a sequence length of 2. Appendix F shows a prediction generated by the best CNN-LSTM model without skip connection. At the bottom of the figure, a MSE difference map is displayed: green regions indicate high accuracy, whereas white or red regions correspond to areas with low accuracy. The difference map clearly highlights that the model performs worst near the melt pool and in regions where the microstructure grains has boundaries. The predicted microstructure also appears more blurred than the ground truth. The blurry-effect occurred because the CNN encoders latent representation, inadvertently lost spatial information for accurately predicting the microstructure grain boundaries.

In an effort to improve the initial model’s ability to predict sharp boundaries, we introduced skip-connection architecture, which provides a direct flow of feature information from the encoder to the decoder. This improved the model’s output significantly (Figure 3). This architectural addition effectively de-blurred the predictions by enabling the decoder to precisely reconstruct the fine-grained spatial detail necessary for microstructure predictions. Since the predictions performed much better with skip-connections, we repeated the experiment of training both CNN-LSTM and PredRNN models with sequence length 2, 3, 4 and 5. The best performing models were again with sequence length 3 and 2 respectively.

Figure 3 shows a prediction produced by the best-performing model with skip-connections, the CNN-LSTM, with a sequence length of 3, applied to the same sample as in Figure 11. Visually, it is clear that the blurred effect has disappeared and that the model has become noticeably better at predicting grain boundaries. Examining the difference map further confirms this improvement: the underlying microstructure is much harder to distinguish, indicating lower error across most of the image. The only region where the model still exhibits higher error is around the melt pool.



Fig. 4. Solidification masks

In an effort to improve this model’s ability to predict the microstructure in the solidification region, we experimented with modifying the loss function. Instead of relying solely on the global MSELoss, we introduced a mask that highlights the temperature interval in which solidification occurs, namely 1560-1620K. A combined loss function was constructed, assigning 30% weight to the global MSELoss and 70% weight to the MSELoss computed only within the solidification region. Figure 4 illustrates the region in which the new loss function assigns a higher weight compared to the rest of the image, for 3 different temperature ranges. Although the metal solidifies within the narrow temperature range of 1560-1620K, this interval is very small. For this reason, we additionally experimented with two broader intervals: 1530-1650K and 1500-1680K.

To establish an upper bound for the microstructure prediction accuracy, we train *MicroNet* using the temperature ground truth for timestep t_{+1} as its input to predict the microstructure at t_{+1} (Section 3.3.2). This allowed us to validate the model’s performance assuming perfect temperature as input. In Section 3.3.3, we predict the microstructure using the *TempNet* predictions for the temperature at t_{+1} as input to the *MicroNet* model to predict the microstructure at t_{+1} .

3.3. Results & Findings

The experiment results were obtained on the DTU GPU Cluster. A dataset split of "12,6,6"-frames (50%,25%,25%) was used throughout.

3.3.1. Temperature

The validation and test performance of the temperature prediction models are summarized in Table 2. For the sequence-length, the model with sequence length 2 (ID1) achieved a validation MSE of 238.23, whereas increasing the sequence length to 4 (ID3) substantially degraded performance, with a validation MSE of 707.92. Reducing the learning rate improved generalization (ID4), with a validation MSE 201.77, while introducing weight decay and reducing the ConvLSTM depth to one layer did not improve test performance. The best overall results were obtained by the model with two ConvLSTM layers and a reduced learning rate (ID7), achieving a validation MSE of 155.87 and a test MSE of 592.60, which

is the lowest among all evaluated configurations. A qualitative visualization of the temperature prediction from this best-performing model is provided in Appendix C.

3.3.2. Microstructure (With Ground Truth Temperature)

To compare the different MicroNet models, we evaluated the normalized mean squared error (NMSE) both globally and within the solidification region. The latter is computed by applying the NMSE loss exclusively to the area where the temperature lies between 1560 and 1620K (See Figure 4). In Table 1, we present the results from 22 different models. Models with IDs 1–3 and 12–14 were trained without skip connections and using only a global MSELoss (Appendix D). Among these, Model 1 with a sequence length of 2 performed the best, achieving a test NMSE of 0.01898 globally and 0.022415 within the solidification region. Models with IDs 4–6 and 15–17 were trained with skip connections but still using only the global MSELoss. In this group, Model 5 with a sequence length of 3 achieved the best performance, with a test NMSE of 0.002884 globally and 0.005733 within the solidification region. Models with IDs 7–11 and 18–22 were trained with both skip connections and the combined loss function. Within this set, Model 19, with a sequence length of 2 and a solidification region between 1530 and 1650K performed the best, achieving a test NMSE of 0.003187 globally and 0.005637 within the solidification region. Model 1 serves as our baseline model. Model 5 represents the best model identified during our attempts to minimize the global NMSE, while Model 19 is the best-performing model from our efforts to improve the NMSE specifically within the solidification region. We compare Models 5 and 19 to the baseline using the following formula in appendix E:

$$\text{NMSE_reduction} = \frac{\text{baseline_NMSE} - \text{model_NMSE}}{\text{baseline_NMSE}} \times 100\%.$$

From this, we find that Model 5 reduces the global NMSE by 84.81% relative to the baseline and reduces the NMSE within the solidification region by 74.42%. Model 19 reduces the global NMSE by 83.21% relative to the baseline and achieves a 74.86% reduction within the solidification region. Thus, the introduction of skip connections significantly lowered both NMSE metrics. The targeted attempt to reduce the NMSE within the solidification region led to only a marginal improvement in that region, while at the same time limiting the reduction in global NMSE.

3.3.3. TempNet + MicroNet

Combining the best Tempnet (Table 2, model ID 7) and MicroNet models (Table 1, model ID 5), we obtain the test prediction loss, NMSE = 0.003003. This NMSE value is slightly higher than the baseline performance of NMSE = 0.002884 achieved by the same MicroNet model

when it was conditioned on the Ground Truth temperature field (T_{t+1}). This difference quantifies the effect of error propagation in our prediction. The use of the predicted temperature field from *TempNet* leads to a measurable NMSE increase of 4.13% for the microstructure prediction, showing the error accumulation from the first stage.

4. DISCUSSIONS

The integration of skip connections into the architecture was important. Its absence in the initial *MicroNet* caused blurred predictions by losing high-frequency spatial features during encoding. The addition of skip connections enabled the precise reconstruction of sharp grain boundaries, significantly reducing the prediction error.

The hypothesis that weighting the loss function towards the solidification region would improve local accuracy was false. Models trained with the combined loss strategy consistently underperformed the MSE baseline, suggesting that restricting the model’s focus introduced gradient instability or hindered the learning of the overall domain dynamics.

The *TempNet* results demonstrated unexpected sensitivity to sequence length. The shortest sequence ($L = 2$) was optimal, while performance degraded for $L = 4$. This result suggests that the temperature dynamics are predominantly dependent only on the immediate past state, or that longer sequences induced overfitting or vanishing gradients. Since L influences the number of model parameters, it is preferable to use the smallest L that does not significantly reduce performance.

5. CONCLUSION

This project showed that deep learning models can predict both temperature fields and microstructure evolution in LBAM with resulting predictions that were physically plausible and visually consistent with expected LBAM phenomena. Skip connections proved essential, enabling sharp spatial reconstructions and greatly reducing error compared to early architectures. The best microstructure model, Model 5, achieved a low global Normalized Mean Squared Error (NMSE) of 0.002884 on the test set. This result demonstrates reliable performance and high predictive accuracy across the majority of the image domain, where the microstructure is considered stable.

The main limitation is the higher error near the solidification front, which neither sequence-length adjustments nor weighted loss functions were able to resolve. Using *TempNet* predictions as input also introduced a small but measurable error increase through the system. Improving performance in the melt region is the key challenge.

Our Github repository is linked here [7], see the Readme file for instructions on reproducing our results.

6. REFERENCES

- [1] Shubo Gao, Zhi Li, Steven Van Petegem, Junyu Ge, Sneha Goel, Joseph Vas, Vladimir Luzin, Zhiheng Hu, H. Seet, D.F. Sanchez, Helena Swygenhoven, Huajian Gao, and Matteo Seita, “Additive manufacturing of alloys with programmable microstructure and properties,” *Nature Communications*, vol. 14, 10 2023.
- [2] Xingjian Shi, Zhourong Chen, Hao Wang, Dit-Yan Yeung, Wai-Kin Wong, and Wang-chun Woo, “Convolutional lstm network: A machine learning approach for precipitation nowcasting,” *Advances in neural information processing systems*, vol. 28, 2015.
- [3] Y. Wang, M. Long, J. Wang, Z. Gao, P. S. Yu, and J. Wang, “Predrnn: Recurrent neural networks for predictive learning using spatiotemporal lstms,” in *Advances in Neural Information Processing Systems*, 2017, vol. 30.
- [4] S.A. Khairallah, A.T. Anderson, A. Rubenchik, and W.E. King, “Laser powder-bed fusion melt-pool dynamics and rapid solidification: prior-effects on microstructure formation,” *Acta Materialia*, vol. 108, pp. 36–45, 2016.
- [5] J. Trapp, H. Naffakh-Moosavy, W. E. King, and A. D. Rollett, “Understanding solidification microstructure in metal additive manufacturing,” *JOM*, vol. 69, pp. 517–522, 2017.
- [6] O. Ronneberger, P. Fischer, and T. Brox, “U-net: Convolutional networks for biomedical image segmentation,” in *Medical Image Computing and Computer-Assisted Intervention – MICCAI 2015*, 2015, vol. 9351, pp. 234–241.
- [7] “Lasernet github repository,” <https://github.com/MadSoeDK/LASERNet>.

The generated output was treated as suggestions, which are heavily reviewed, edited and adapted before integrating them into the codebase or report.

DECLARATION OF USE OF GENERATIVE AI

We used generative AI tools for this project. The following two sections describe the tools, what it was used for, what stage of the process we used the tool and how we used or incorporated the output.

ChatGPT was used for various tasks throughout the project. Especially in the research phase, it was used to help us understand theory related to how microstructure and IPF are related. For report-writing the tool was used for grammar checking and for rephrasing sentences when needed. Claude Code was used primarily in the early stages to help create the dataloader and the preprocessing pipeline, since it excels at tasks like that. We could get the basics set up so we could focus on modelling the problem ourselves. Claude Code is also excellent at generating code for creating nicely formatted plots and tables from our results, which we also used it for.

A. FINAL RESULT TABLES

Table 1. Microstructure Model Comparison Summary (NMSE = Loss). Best model (lowest test error) marked with bold.

ID	Name	Train NMSE	Val NMSE	Val Solid NMSE	Test NMSE	Test Solid NMSE	Epochs
1	01_MICROnet.cnn.lstm.seq2.MSELoss_no_skip	0.013510	0.016581	0.020046	0.018980	0.022415	200
2	02_MICROnet.cnn.lstm.seq3.MSELoss_no_skip	0.012927	0.016816	0.020126	0.019636	0.023232	200
3	03_MICROnet.cnn.lstm.seq4.MSELoss_no_skip	0.014326	0.017720	0.021294	0.020498	0.024384	200
4	04_MICROnet.cnn.lstm.seq2.MSELoss	0.001912	0.002976	0.005646	0.003172	0.006328	125
5	05_MICROnet.cnn.lstm.seq3.MSELoss	0.001799	0.002801	0.005490	0.002884	0.005733	127
6	06_MICROnet.cnn.lstm.seq4.MSELoss	0.002489	0.003415	0.006253	0.004332	0.007532	113
7	07_MICROnet.cnn.lstm.seq3.CombLoss_T1560-1620_s70_g30	0.003756	0.006806	0.007779	0.004993	0.007926	70
8	08_MICROnet.cnn.lstm.seq3.CombLoss_T1530-1650_s70_g30	0.002796	0.004553	0.004965	0.003906	0.006772	103
9	09_MICROnet.cnn.lstm.seq3.CombLoss_T1500-1680_s70_g30	0.002422	0.004772	0.005375	0.003476	0.006629	135
10	10_MICROnet.cnn.lstm.seq3.CombLoss_T1560-1620_s50_g50	0.003655	0.008849	0.010732	0.005126	0.007917	73
11	11_MICROnet.cnn.lstm.seq3.CombLoss_T1560-1620_s30_g70	0.003002	0.007579	0.010063	0.004491	0.007376	93
12	12_MICROnet.predrnn.seq2.MSELoss_no_skip	0.010434	0.018856	0.025464	0.029668	0.036360	200
13	13_MICROnet.predrnn.seq3.MSELoss_no_skip	0.012358	0.021446	0.027430	0.030586	0.037629	200
14	14_MICROnet.predrnn.seq4.MSELoss_no_skip	0.013186	0.020897	0.025921	0.026787	0.032924	200
15	15_MICROnet.predrnn.seq2.MSELoss	0.001950	0.002948	0.004969	0.002892	0.005560	133
16	16_MICROnet.predrnn.seq3.MSELoss	0.002273	0.003550	0.005207	0.003367	0.005902	112
17	17_MICROnet.predrnn.seq4.MSELoss	0.002536	0.003518	0.005661	0.003569	0.006399	177
18	18_MICROnet.predrnn.seq2.CombLoss_T1560-1620_s70_g30	0.003607	0.008160	0.008865	0.004951	0.007479	82
19	19_MICROnet.predrnn.seq2.CombLoss_T1530-1650_s70_g30	0.003069	0.005013	0.005945	0.003187	0.005637	126
20	20_MICROnet.predrnn.seq2.CombLoss_T1500-1680_s70_g30	0.004283	0.005662	0.006555	0.003973	0.006274	109
21	21_MICROnet.predrnn.seq2.CombLoss_T1560-1620_s50_g50	0.003359	0.005607	0.006772	0.003969	0.006699	78
22	22_MICROnet.predrnn.seq2.CombLoss_T1560-1620_s30_g70	0.003990	0.008379	0.012095	0.006496	0.009353	58

Table 2. Temperature Model Results (MSE and MAE for Validation and Test). Best model (lowest test error) marked with bold.

ID	Name	Val MSE	Val MAE	Test MSE	Test MAE	Epochs
1	T01_seq2_lr1e-3	238.2337	9.8101	1473.9021	29.0843	200
2	T02_seq3_lr1e-3	331.5028	11.9782	864.6430	21.3301	200
3	T03_seq4_lr1e-3	707.9156	20.1695	1425.7248	33.5815	200
4	T04_seq2_lr6e-4	201.7720	9.2024	852.6385	18.3784	200
5	T05_seq2_lr1e-3_wd1e-5	284.4843	11.2322	1589.8728	29.3443	200
6	T06_seq2_lr1e-3_1layer	174.4407	10.0587	1826.9046	36.0405	200
7	T07_seq2_lr5e-4_2layers	155.8687	9.1100	592.5967	19.2897	200
8	T08_seq2_wider_channels	286.7250	11.2165	710.0041	20.8788	200

B. TEMPNET EXPERIMENT RESULTS

This appendix contains the detailed results of the temperature model tuning experiments, including the training and validation performance table, loss curve visualizations, and qualitative prediction outputs for the evaluated architectures.

Table 3. Temperature Model Results for Architecture Tuning (Training and Validation)

ID	Description	Train MSE	Train MAE	Val MSE	Val MAE	Epochs
T1	Baseline (3 conv, 1 LSTM layer, seq-length 3)	946.1887	17.57	4002.1246	36.08	200
T2	Baseline + U-Net	1836.6469	23.33	1711.0694	33.14	200
T3	Baseline + U-Net + 4 conv	2391.6065	25.62	1051.3666	19.03	200
T4	Baseline + U-Net + 4 conv + 2 LSTM layers	704.0708	12.93	806.0829	22.52	300
T5	Baseline + U-Net + 4 conv + 2 LSTM layers + Dropout	6895.6562	41.02	902.4702	23.06	300
T6	Baseline + U-Net + 4 conv + 2 LSTM + L1 loss	31976.2805	78.11	9841.2740	40.37	300
T9	Baseline + U-Net + 4 conv + 2 LSTM + Smooth L1	819.8585	17.47	4992.5581	50.30	300

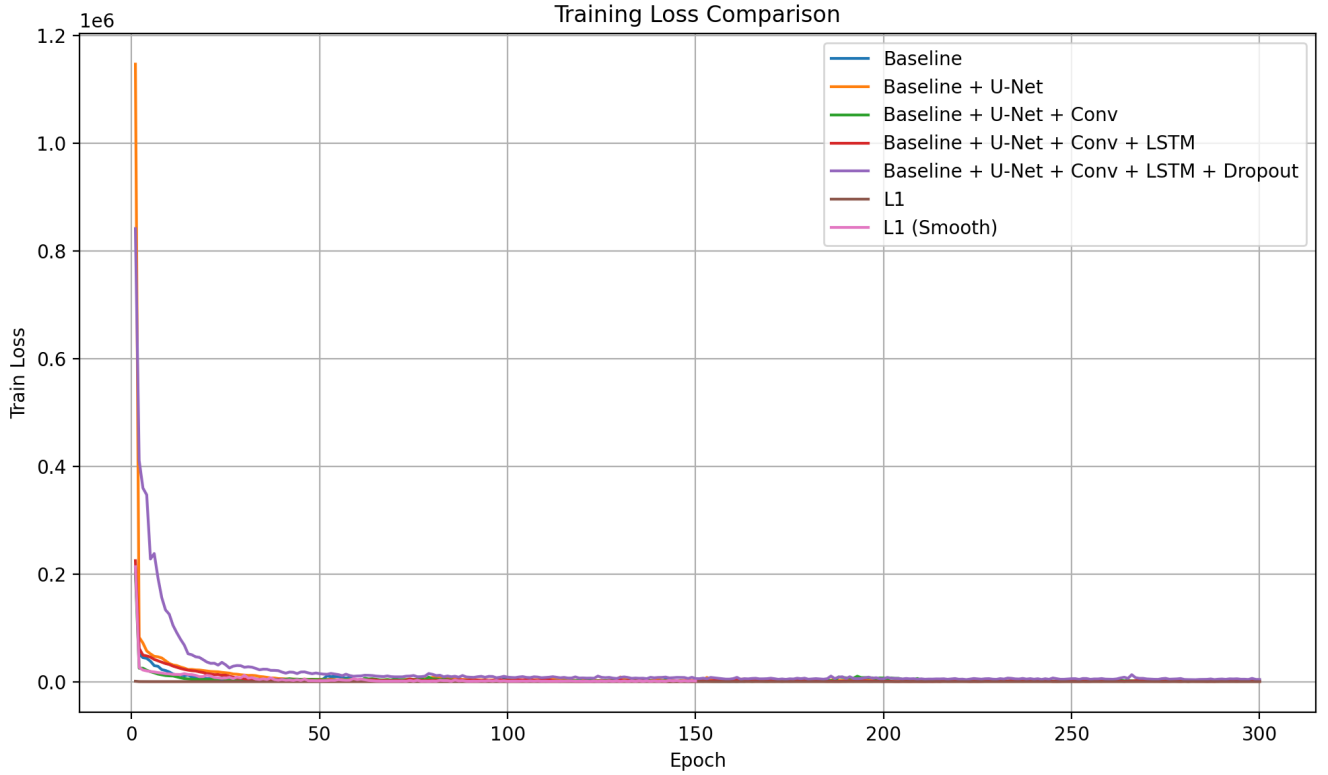


Fig. 5. Training losses for the different models tested during tuning.

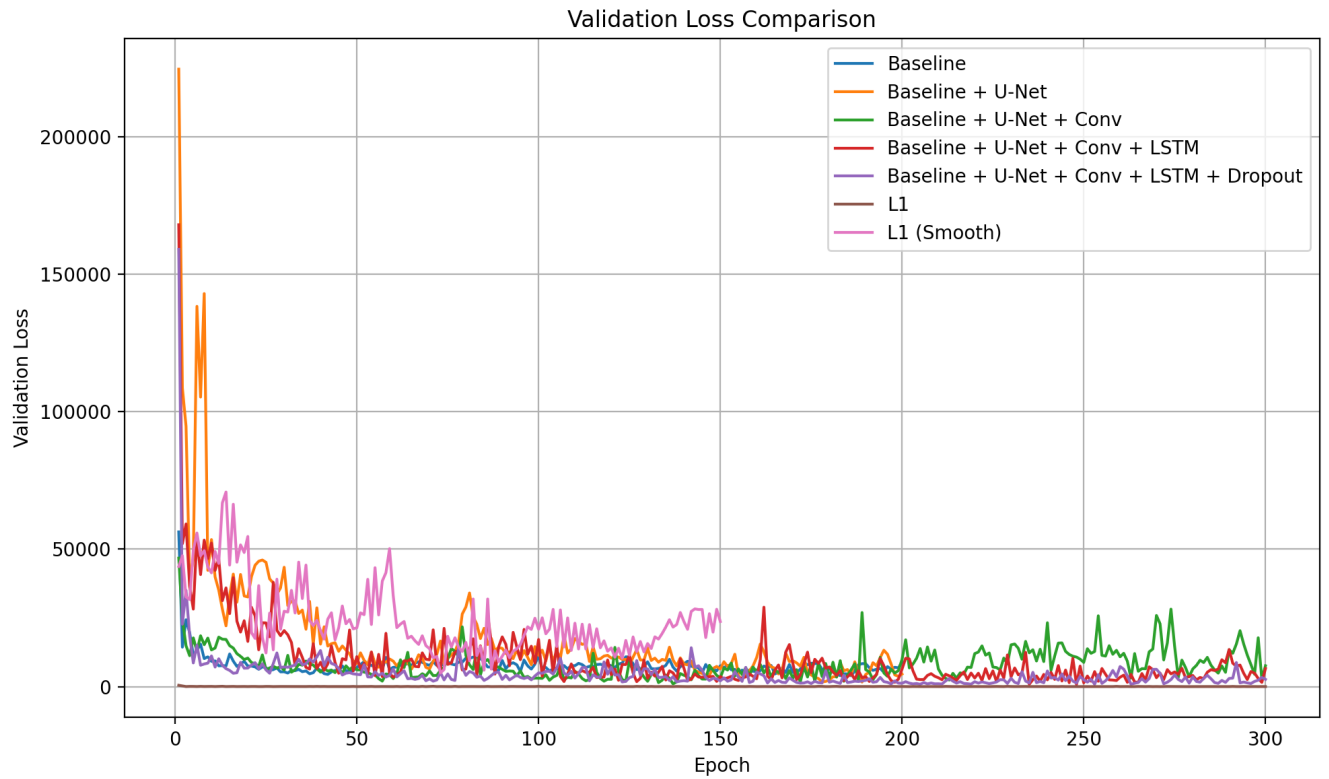


Fig. 6. Validation losses for the different models tested during tuning.

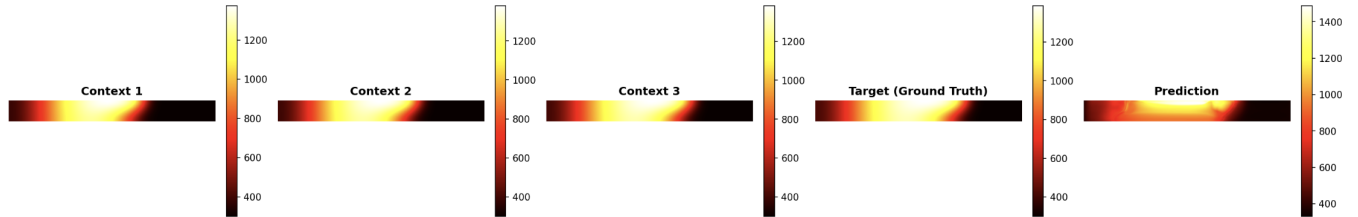


Fig. 7. Test set predictions, CNN-LSTM baseline (Table 3, ID T1) for TempNet with sequence length 3. The 5 frame are the following timesteps $t_{20}, t_{21}, t_{22}, t_{23}, \hat{t_{23}}$.

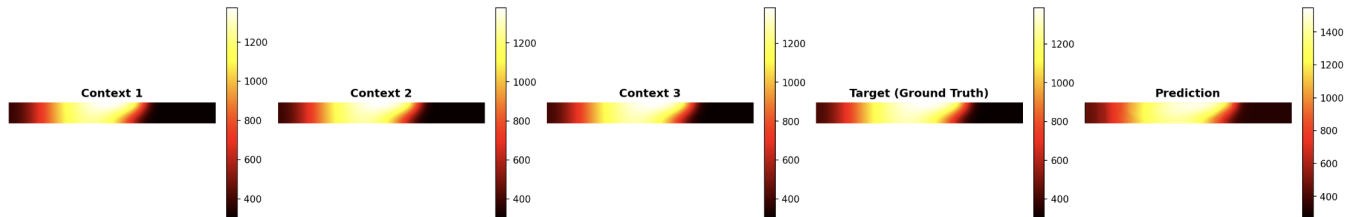


Fig. 8. Test set predictions, best CNN-LSTM (Table 3, ID T4) baseline for TempNet with sequence length 3. The 5 frame are the following timesteps $t_{20}, t_{21}, t_{22}, t_{23}, \hat{t_{23}}$.

C. BEST TEMPNET PREDICTION - VISUALIZATION RESULTS

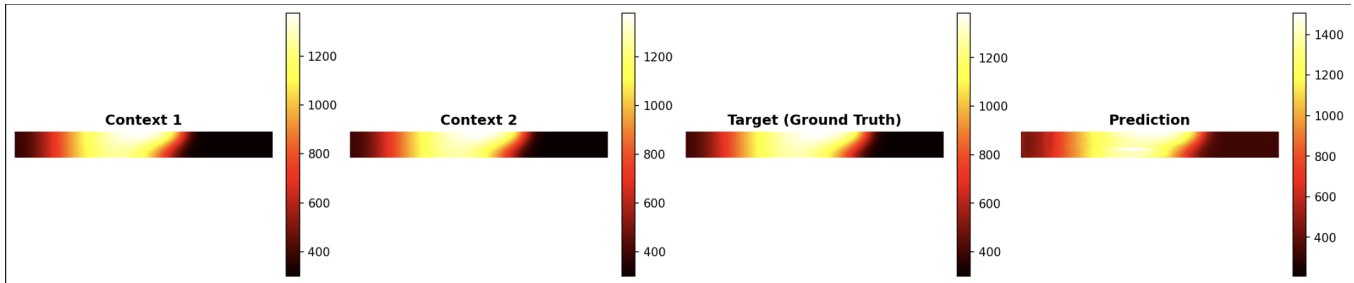


Fig. 9. Test set predictions for the best TempNet model (Table 2, ID 7). The 4 frame are the following timesteps $t_{20}, t_{21}, t_{22}, \hat{t}_{22}$

D. MICRONET TRAINING LOSS CURVE

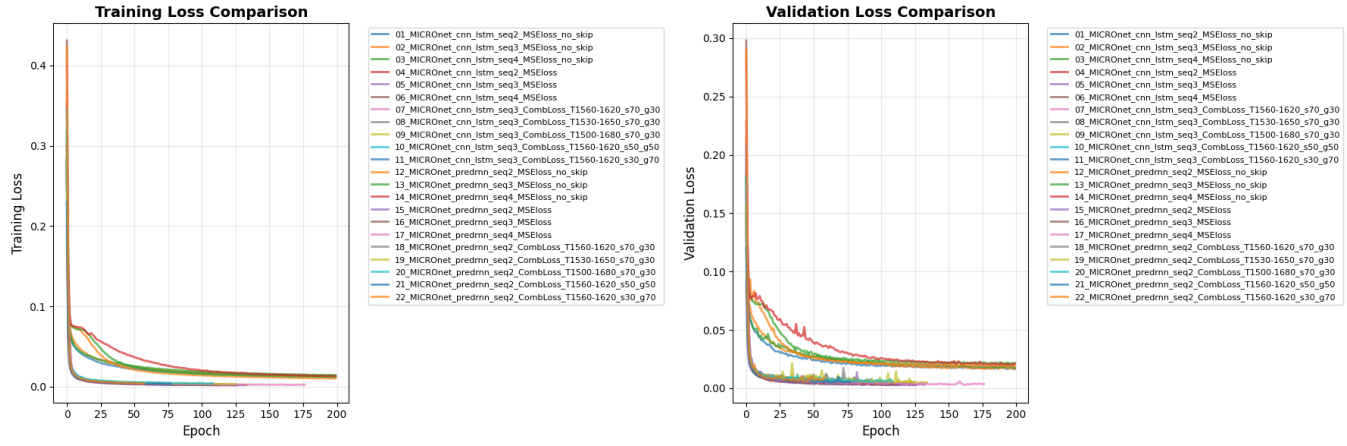


Fig. 10. MicroNet training loss curves

E. NMSE REDUCTION CALCULATIONS

This appendix presents the detailed NMSE reduction calculations for the baseline model (Model 1) and the two improved models (Model 5 and Model 19).

E.1. Baseline Model (Model 1)

$$\text{NMSE}_{1,\text{global}} = 0.01898, \quad \text{NMSE}_{1,\text{solid}} = 0.022415$$

E.2. Model 5: Global MSELoss With Skip Connections

E.2.0.1. Global NMSE

$$\text{NMSE}_{5,\text{global}} = 0.002884$$

$$\text{NMSE_reduction}_{5,\text{global}} = \frac{0.01898 - 0.002884}{0.01898} \times 100\% = 84.81\%.$$

E.2.0.2. Solidification Region NMSE

$$\text{NMSE}_{5,\text{solid}} = 0.005733$$

$$\text{NMSE_reduction}_{5,\text{solid}} = \frac{0.022415 - 0.005733}{0.022415} \times 100\% = 74.42\%.$$

E.3. Model 19: Combined Loss With Skip Connections

E.3.0.1. Global NMSE

$$\text{NMSE}_{19,\text{global}} = 0.003187$$

$$\text{NMSE_reduction}_{19,\text{global}} = \frac{0.01898 - 0.003187}{0.01898} \times 100\% = 83.21\%.$$

E.3.0.2. Solidification Region NMSE

$$\text{NMSE}_{19,\text{solid}} = 0.005637$$

$$\text{NMSE_reduction}_{19,\text{solid}} = \frac{0.022415 - 0.005637}{0.022415} \times 100\% = 74.86\%.$$

F. MICRONET PREDICTION WITHOUT SKIP CONNECTIONS

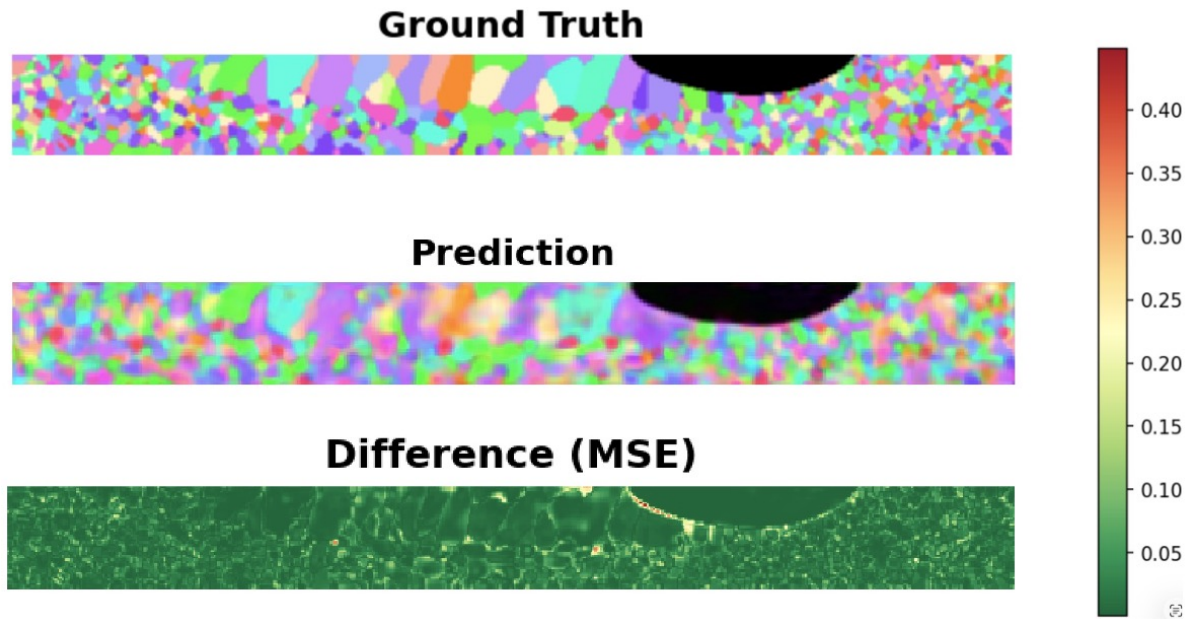


Fig. 11. CNN-LSTM baseline (without skip connections) with sequence length 3. $T = t_{23}$, y-axis slice index 47.